1

2

Title: Bone-Inspired Microarchitectured Materials with Enhanced Fatigue Life

4

5   **Authors:** Ashley M. Torres[1,2], Adwait A. Trikanad[3], Cameron A. Aubin[1], Floor M. Lambers[1], Marysol

6   Luna[1], Clare M. Rimnac[4], Pablo Zavattieri[3], Christopher J. Hernandez[1,2,5*]

7   **Affiliations:**

8   [1]Sibley School of Mechanical and Aerospace Engineering, Cornell University, Ithaca, NY, USA.

9   [2]Meinig School of Biomedical Engineering, Cornell University, Ithaca, NY, USA.

10   [3]Lyles School of Civil Engineering, Purdue University, West Lafayette, IN, USA.

11   [4]Department of Mechanical & Aerospace Engineering, Case Western Reserve University, Cleveland,

12   OH, USA.

13   [5]Hospital for Special Surgery, New York, NY, USA.

14   *Correspondence to: cjh275@cornell.edu

15

16

Text 1

17   **Microarchitectured materials achieve superior mechanical properties through geometry**

18   **rather than composition [1-4]. Although lightweight, high-porosity microarchitectured materials can**

19   **have high stiffness and strength, stress concentrations within the microstructure can cause flaw**

20   **intolerance under cyclic loading [5,6], limiting fatigue life. However, it is not known how**

21   **microarchitecture contributes to fatigue life. Naturally occurring materials can display**

22   **exceptional mechanical performance and are useful models for the design of microarchitectured**

23   **materials [7,8]. Cancellous bone is a naturally occurring microarchitectured material that often**

24   **survives decades of habitual cyclic loading without failure. Here we show that resistance to fatigue**

25   **failure in cancellous bone is sensitive to the proportion of material oriented transverse to applied**

26   **loads – a 30% increase in density caused by thickening transversely oriented struts increases**

27   **fatigue life by 10-100 times. This finding is surprising in that transversely oriented struts have**

28   **negligible effects on axial stiffness, strength and energy absorption. The effects of transversely**

29   **oriented material on fatigue life are also present in synthetic lattice microstructures. In both**

30   **cancellous bone and synthetic microarchitectures, the fatigue life can be predicted using the**

31   **applied cyclic stress after adjustment for apparent stiffness and the proportion of the**

32   **microstructure oriented transverse to applied loading. In the design of microarchitectured**

33   **materials, stiffness, strength and energy absorption is often enhanced by aligning the**

34   **microstructure in a preferred direction. Our findings show that introduction of such anisotropy,**

35   **by reducing the amount of material oriented transverse to loading, comes at the cost of reduced**

36   **fatigue life. Fatigue failure of durable devices and components generates substantial economic**

37   **costs associated with repair and replacement. As advancements in additive manufacturing expand**

38   **the use of microarchitectured materials to reusable devices including aerospace applications, it is**

39   **increasingly necessary to balance the need for fatigue life with those of strength and density.**

Text 2

40   Fatigue failure is caused by the accumulation of microscopic damage following repeated loading

41 and generates substantial economic costs associated with repair and replacement of durable devices.

42 Microarchitectured materials are particularly susceptible to fatigue failure because the complex

43 geometry can result in local stresses an order of magnitude greater than stresses applied to the bulk

44 material [5,6,9]. The presence of large stress concentrations can promote damage initiation and

45 accumulation under cyclic loading and thereby reduce the fatigue life. Naturally occurring

46 microarchitectured materials also experience cyclic loading and provide a model for strategies to resist

47 fatigue failure.

48   Bone is a biological material with high stiffness and strength relative to density. In humans, most

49 bones survive more than 50 years of habitual loading without failure. Whole bones consist of an outer

50 shell made of dense tissue known as cortical bone that surrounds a foam-like tissue known as cancellous

51 bone. Cancellous bone consists of a network of interconnected plate-like and rod-like struts called

52 trabeculae (~50-300 μm in thickness). Trabeculae in cancellous bone are preferentially aligned in the

53 direction of stresses generated by habitual physical activity, resulting in a transversely isotropic

54 microstructure. The fatigue life of cancellous bone and other cellular solids follows a normalized stress

55 v. life (S-N) relationship under cyclic compressive loading [10]:

56
$$\frac{\sigma}{E_0} = A N_f^B, \tag{1}$$

57 where σ is the maximum compressive stress, E_0 is the initial Young's modulus, N_f is the number of

58 cycles to failure, and A and B are empirical constants.

59   To better understand the effects of microarchitecture on fatigue life, we determined the

60 relationship between microstructure and fatigue damage processes in high porosity ($> 90\%$) cancellous

61 bone from the vertebral bodies of deceased human donors (n=44 specimens from 18 donors, see

Text 3

62   Methods). Cyclic compressive loading (zero to compression) was applied in the direction of habitual

63   loading in vivo. Fatigue loading was suspended at a specified amount of cyclic loading (determined by

64   accumulated cyclic strain) and the resulting amount and location of damage within the microstructure

65   was detected using contrast agents (Fig. 1a and 1b, see Methods)[11,12]. Microarchitecture was assessed

66   using three-dimensional images and analyzed using a morphological decomposition approach that

67   isolates each individual strut within the structure and classifies the strut as plate-like or rod-like as well

68   as determining its orientation relative to loading (Fig. 1c, d, see Methods)[13]. The amount of tissue

69   damage caused by fatigue loading was correlated with maximum applied apparent strain (Extended Data

70   Table S1) but was not correlated with specimen density or other specimen-average measures of

71   microstructure. Surprisingly, the amount of tissue damage was reduced in specimens with thicker rod-

72   like struts (Fig. 1e, Extended Data Table S2, $R^2=0.76$, $p < 0.01$). This finding was unexpected since rod-

73   like struts in cancellous bone constitute, on average, only 20% of the solid volume of high porosity

74   cancellous bone (Extended Data Table S3) are primarily oriented transversely, carry only a small

75   proportion of longitudinally-oriented loads, and therefore have negligible effects on stiffness and

76   strength in the longitudinal direction [14] (transversely oriented elements have similar, small effects in
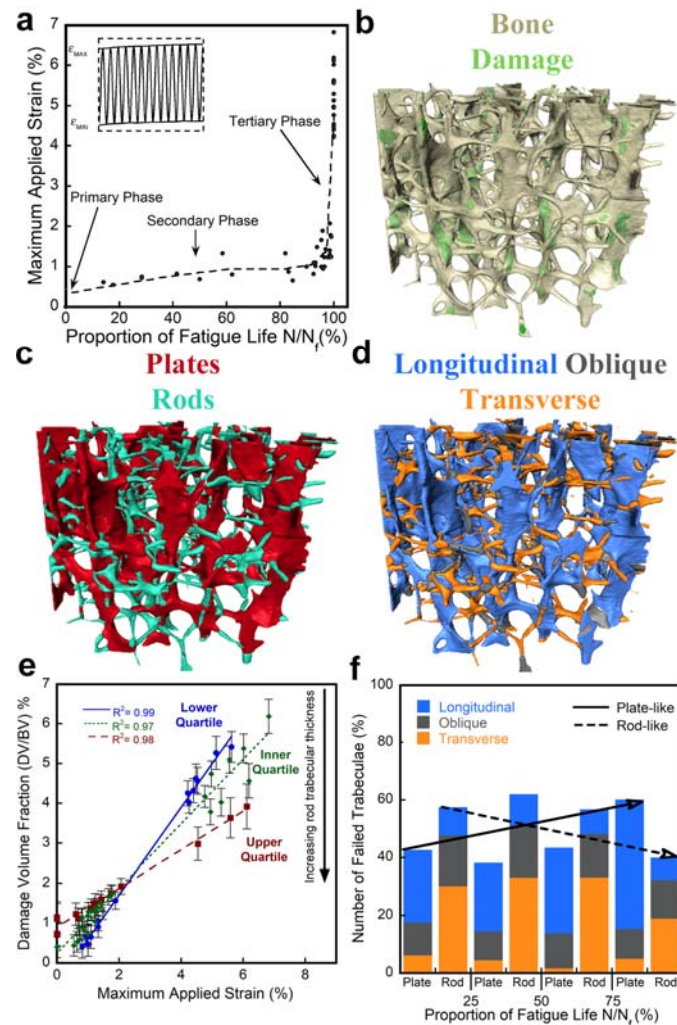
77   nanolattice structures [15]).

Text 4

Fig. 1. Microarchitecture influences fatigue damage accumulation in cancellous bone. a, The creep-fatigue curve of cancellous bone is shown with the three phases of fatigue loading indicated. Cyclic compressive loading of cancellous bone was stopped at different points along the creep fatigue curve (data points) to determine patterns of damage accumulation. Three dimensional images of cancellous bone with **b,** green indicating damage, **c,** plate-like and rod-like struts and **d,** strut orientation relative to anatomical position (longitudinal, oblique, and transverse). **e,** The amount of damage in cancellous bone was correlated with maximum applied strain, but specimens with thicker rod-like trabeculae experienced less damage accumulation (R^2=0.76, $p < 0.01$). Error bars

Text 5

88   indicate the standard deviation as determined from the linear mixed effects model. **f.**

89   Early in fatigue life, strut failure occurs primarily in transversely oriented rod-like struts;

90   final mechanical failure is characterized by widespread failure of longitudinally oriented

91   plate-like struts.

92

93   To better understand the effect of rod-like struts on fatigue failure we examined the distribution

94   of tissue damage at different points during the fatigue loading process. Early in fatigue, failure of struts

95   occurs primarily in rod-like trabeculae; substantial damage accumulation in plate-like trabeculae does

96   not occur until overt failure (Fig. 1f). The pattern of strut failure is also related to orientation, failed rod-

97   like trabeculae are predominately transversely oriented while failed plate-like trabeculae are

98   predominately oriented longitudinally (Extended Data Fig. S1). The experimental findings were

99   consistent with finite element models that indicated that apparent compressive loading results in tensile

100   stresses in rod-like trabeculae (primarily transversely oriented) and compressive stresses in plate-like

101   trabeculae (primarily longitudinally oriented, Extended Data Fig. S2). These findings suggest that, in

102   cancellous bone, transversely oriented trabeculae act as sacrificial elements during cyclic loading by

103   accumulating tissue damage and thereby protecting the load carrying, longitudinally oriented, plate-like

104   trabeculae.

105   Tissue heterogeneity is also a major contributor to damage accumulation in cancellous bone [12,16]

106   and is therefore a potential explanation for our findings in human bone tissue. To confirm that the effects

107   of transversely oriented struts was due to geometry rather than material heterogeneity we generated three

108   dimensional models of cancellous bone microstructures using a high-resolution projection

109   stereolithography printer (Fig. 2 a,b, M1, Carbon, USA) and a urethane methacrylate resin (UMA) [17].

110   Cancellous bone microstructures (Fig. 2b, n=5) were modified by adding material to the surface of

Text 6

111   transverse trabeculae in one of three increments: no modification (original geometry), +20 µm on the

112   surface (an average increase in rod thickness of 20% ± 5%, mean ± SD), or +60 µm on each surface (an

113   average increase in rod thickness of 45% ± 14%). Because transverse rod-like trabeculae constitute only

114   a small portion of the solid volume and carry only a small portion of loads due to their orientation,

115   thickening of rod-like struts had only a small effect on density (Fig. 2c, increase of 11% ± 8%, mean ±

116   SD) and apparent stiffness (22% ± 19% increase in longitudinal Young's modulus, Fig. 2d). However,

117   these small increases in thickness of rod-like trabeculae led to increases in fatigue life by as much as two

118   orders of magnitude (Fig. 2e, Extended Data Fig. S3).

119   To confirm that damage accumulation in the 3D printed models was similar to that of cancellous

120   bone, we examined damage in the microstructure using a radio-opaque dye penetrant (Fig. 2f). Printed

121   specimens with thicker rod-like struts showed reduced damage accumulation (Fig. 2g). Hence,

122   localization of failure in the printed models matched the patterns seen in cancellous bone, suggesting

123   similar failure mechanisms among materials and further supporting the idea that increases in fatigue life

124   are due to changes in microarchitecture and not material heterogeneity. Furthermore, finite element

125   models of the specimens indicated that the average stresses in rod-like trabeculae (predominately

126   transversely oriented) were greater than those in plate-like trabeculae (predominately longitudinally

127   oriented, Extended Data Fig. S2), demonstrating the localization of damage follows load distributions

128   within the microarchitecture. Together these findings indicate that small increases in mass applied to

129   transversely oriented structural components of the microstructure can reduce matrix stresses leading to

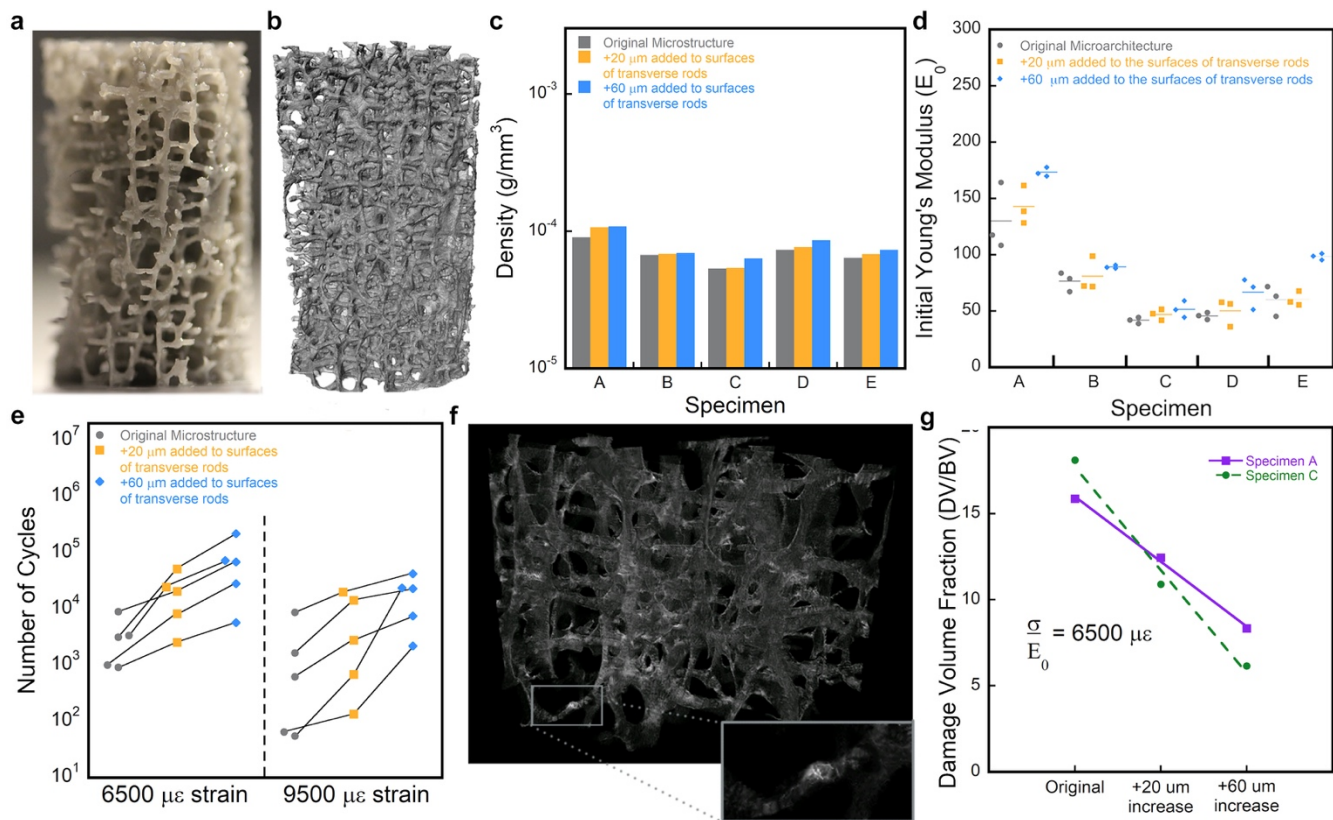130   disproportionately large, beneficial effects on fatigue life.

131

Text 7

Fig. 2 | Models of cancellous bone generated using additive manufacturing show that fatigue life is sensitive to small changes in microarchitecture. **a,** digital images of human vertebral cancellous bone were edited and printed into **b.** high-resolution three-dimensional models. Increases in the thickness rod-like struts had small effects on **c,** density, and **d.** stiffness (Young's modulus in first cycle of loading), yet resulted in **e,** increases in fatigue life by as much as 2 orders of magnitude (lines connect samples derived from the same bone specimen, two magnitudes of normalized cyclic stress are shown). **f,** A micro-computed tomography image of a three-dimensional printed sample of cancellous bone after fatigue loading to failure. A radio-opaque dye penetrant indicated regions of accumulated damage. **g,** The amount of damage generated by fatigue loading to failure was reduced in 3D printed specimens with greater thickness of rod-like struts.

Text 8

145

146   To determine if the effects of transverse elements on fatigue failure are generalizable to other

147   cellular solids, we created printed models of an octet truss [1] as well as an octet truss modified to have

148   plate-like and rod-like elements mimicking the microstructure and anisotropy of cancellous bone (Fig.

149   3a). The octet truss shows a stretching dominated deformation behavior, cancellous bone microstructure

150   shows bending dominated behavior and the bone-like microarchitecture displayed a combination of both

151   stretching and bending deformation behaviors (Extended Data Fig S4). In the bone-like

152   microarchitectures, increases in transverse strut thickness resulted in an increase in the fatigue life by a

153   factor of eight (Fig. 3b) with only a small change in density (+4%) or longitudinal stiffness (+20%,

154   Extended Data Table S4). In the octet truss, increases in transverse strut thickness resulted in an increase

155   in fatigue life by a factor of five (Fig. 3b) with only minor changes in density (+10%) or uniaxial

156   stiffness (+14%, Fig. 3b, Extended Data Table S4). In contrast, when the orientation of the octet trusses

157   with thickened elements was rotated by 90 degrees so that thickened elements were oblique to the

158   applied loads, the fatigue life was *reduced* by a factor of 9 (Fig. 3b), demonstrating that the effect of

159   transverse struts on fatigue life is related to the proportion of material oriented transverse to loading

160   rather than the thickness of the transverse struts *per se*. To understand the extent to which the

161   transversely oriented material influenced fatigue damage accumulation we performed nonlinear finite

162   element models of cyclic loading. Fatigue damage involves a local irreversible energy dissipating

163   process resulting in increases in inelastic dissipation energy. Finite element models of cyclic loading

164   indicate that the fatigue life of the octet and bone-like microarchitectures with and without thickened

165   struts is closely related to the inelastic dissipation energy per unit work (Fig. 3c). Hence, increases in the

166   transverse volume fraction (ψ, the proportion of the solid volume oriented transverse to loading) in these

167   microarchitectured materials reduce the amount of inelastic energy dissipation and damage

Text 9

168   accumulation during cyclic loading, just as thicker rod-like trabeculae (predominately transversely

169   oriented) experienced less damage accumulation in cancellous bone (Fig 1e). Together these findings

170   show that the effects of transverse struts on fatigue life is not unique to cancellous bone but extends to

171   synthetic microarchitectured materials. That our findings regarding damage accumulation are consistent

172   in human bone tissue (a biological ceramic polymer composite) as well as a polymer used in additive

173   manufacturing further suggests that the effect is due to geometry and is not limited to one class of

174   constituent material.

175   We developed empirical models to characterize the relationship between fatigue life (N_f), applied

176   cyclic normalized stress (noted as σ/E_0 for cellular solids), and transverse volume fraction (ψ) for bone,

177   bone-like microarchitectures and octet trusses. Surprisingly, the regression models identified a

178   predictive equation only slightly different from (1):

179
$$\frac{\sigma}{E_0}\frac{1}{\sqrt{\psi}} = A N_f^B, \qquad\qquad (2)$$

180   in which A and B are empirical constants ($R^2 = 0.82$, Fig. 3d, Extended Data Table S5). This simple

181   modification to the normalized S-N relationship provides a means of considering fatigue life during the

182   design of microarchitectured materials. Designs with greater proportions of struts aligned axial to

183   loading are more efficient in terms of specific stiffness and strength [15], but will also experience reduced

184   fatigue life due to reductions in the proportion of material oriented transverse to expected loading.

185   Future applications of high porosity microarchitectured materials to durable products such as vehicles

186   will require balancing performance in terms of stiffness, strength and energy absorption with costs

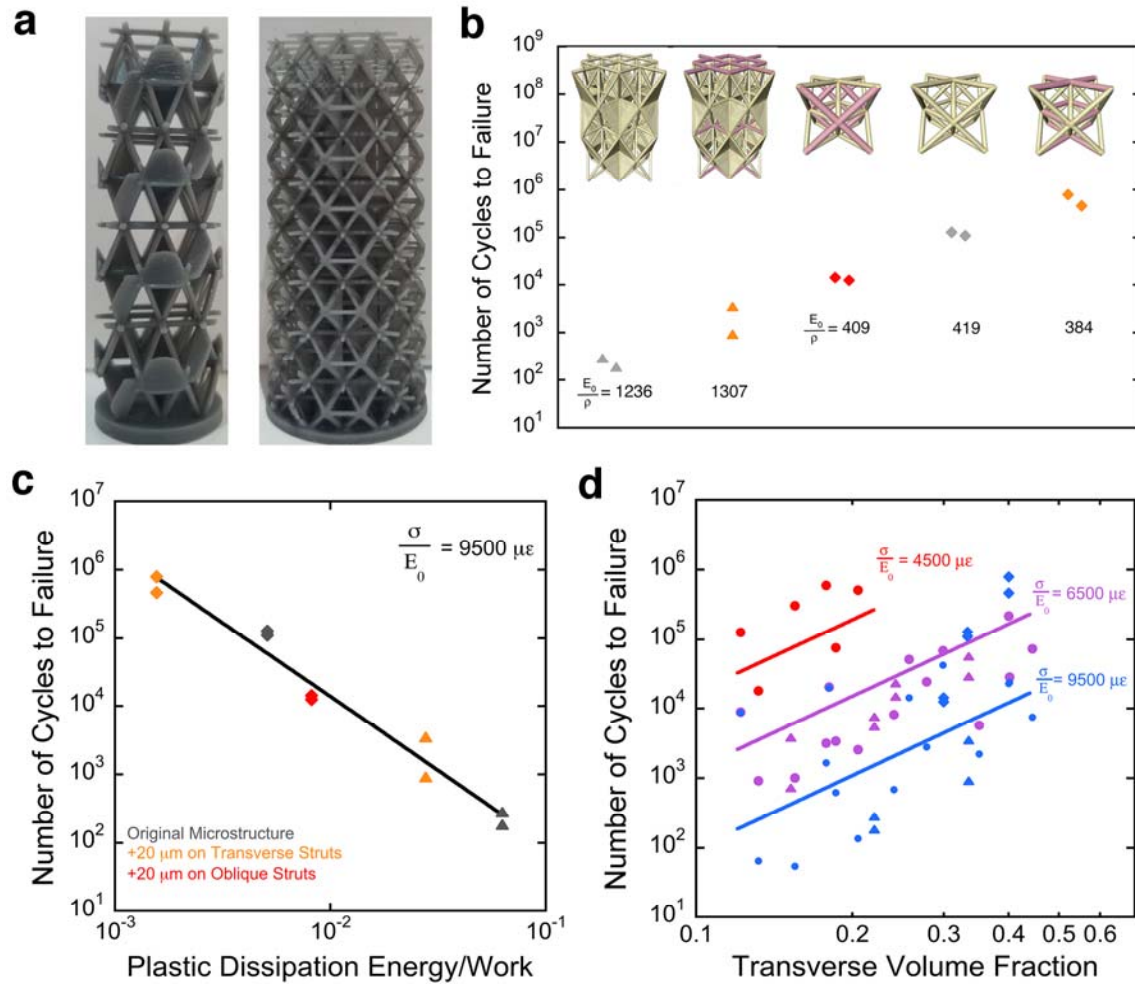187   associated with replacement and repair due to fatigue failure.

188

189

190

191   **Fig. 3 Transverse volume influences fatigue life in repeating cellular solids. a,** Images

192   of the bone-inspired microstructure and an octet truss are shown. **b,** The fatigue life of

193   microarchitectured materials printed as designed or with rod-like struts thickened

194   (colored) is shown. Thickening transverse struts increases fatigue life, while thickening

195   vertically oriented struts reduces fatigue life (specific stiffness, E_0/ρ is also shown). **c,**

196   Fatigue life of the lattice structures is related to the inelastic dissipation energy per unit

197   work determined from finite element models. **d,** Fatigue life for 3D printed specimens of

198   bone (•), bone-like microstructure (▲) and octets (♦) at different applied cyclic loading

199   (σ/E_0, noted in $\mu\varepsilon$). Lines indicate the regression model fits (Equation 2, $R^2 = 0.82$).

Text 11

200

201   **Supplementary Information** is linked to the online version of the paper

202

203   **References:**

204   1   Zheng, X. *et al.* Ultralight, ultrastiff mechanical metamaterials. *Science* **344**, 1373-1377,

205   doi:10.1126/science.1252291 (2014).

206   2   Berger, J. B., Wadley, H. N. & McMeeking, R. M. Mechanical metamaterials at the theoretical

207   limit of isotropic elastic stiffness. *Nature* **543**, 533-537, doi:10.1038/nature21075 (2017).

208   3   Bauer, J., Hengsbach, S., Tesari, I., Schwaiger, R. & Kraft, O. High-strength cellular ceramic

209   composites with 3D microarchitecture. *P Natl Acad Sci USA* **111**, 2453-2458,

210   doi:10.1073/pnas.1315147111 (2014).

211   4   Fleck, N. A., Deshpande, V. S. & Ashby, M. F. Micro-architectured materials: past, present and

212   future. *P Roy Soc a-Math Phy* **466**, 2495-2516, doi:10.1098/rspa.2010.0215 (2010).

213   5   Jang, D. C., Meza, L. R., Greer, F. & Greer, J. R. Fabrication and deformation of three-

214   dimensional hollow ceramic nanostructures. *Nature Materials* **12**, 893-898,

215   doi:10.1038/Nmat3738 (2013).

216   6   Xiong, J. *et al.* Advanced Micro-Lattice Materials. *Advanced Engineering Materials* **17**, 1253-

217   1264, doi:10.1002/adem.201400471 (2015).

218   7   Meyers, M. A., McKittrick, J. & Chen, P. Y. Structural biological materials: critical mechanics-

219   materials connections. *Science* **339**, 773-779, doi:10.1126/science.1220854 (2013).

220   8   Wegst, U. G., Bai, H., Saiz, E., Tomsia, A. P. & Ritchie, R. O. Bioinspired structural materials.

221   *Nat Mater* **14**, 23-36, doi:10.1038/nmat4089 (2015).

222   9   Shen, H., Li, H. & Brinson, L. C. Effect of microstructural configurations on the mechanical

223 responses of porous titanium: A numerical design of experiment analysis for orthopedic

224 applications. *Mech. Mater.* **40**, 708-720, doi:10.1016/j.mechmat.008.03.009 (2008).

225 10 Haddock, S. M., Yeh, O. C., Mummaneni, P. V., Rosenberg, W. S. & Keaveny, T. M. Similarity

226 in the fatigue behavior of trabecular bone across site and species. *J. Biomech.* **37**, 181-187

227 (2004).

228 11 Lambers, F. M., Bouman, A. R., Rimnac, C. M. & Hernandez, C. J. Microdamage caused by

229 fatigue loading in human cancellous bone: relationship to reductions in bone biomechanical

230 performance. *PLoS One* **8**, e83662, doi:10.1371/journal.pone.0083662 (2013).

231 12 Torres, A. M. *et al.* Material heterogeneity in cancellous bone promotes deformation recovery

232 after mechanical failure. *Proc Natl Acad Sci U S A* **113**, 2892-2897,

233 doi:10.1073/pnas.1520539113 (2016).

234 13 Liu, X. S. *et al.* Complete volumetric decomposition of individual trabecular plates and rods and

235 its morphological correlations with anisotropic elastic moduli in human trabecular bone. *J. Bone*

236 *Miner. Res.* **23**, 223-235 (2008).

237 14 Liu, X. S., Zhang, X. H. & Guo, X. E. Contributions of trabecular rods of various orientations in

238 determining the elastic properties of human vertebral trabecular bone. *Bone* **45**, 158-163,

239 doi:10.1016/j.bone.2009.04.201 (2009).

240 15 Meza, L. R. *et al.* Resilient 3D hierarchical architected metamaterials. *Proc Natl Acad Sci U S A*

241 **112**, 11502-11507, doi:10.1073/pnas.1509120112 (2015).

242 16 Tertuliano, O. A. & Greer, J. R. The nanocomposite nature of bone drives its strength and

243 damage resistance. *Nat Mater* **15**, 1195-1202, doi:10.1038/nmat4719 (2016).

244 17 Tumbleston, J. R. *et al.* Continuous liquid interface production of 3D objects. *Science* **347**, 1349-

245 1352, doi:10.1126/science.aaa2397 (2015).

Text 13

246

247

259

260   **Competing interests:** The authors declare no competing interests.

261   Correspondence and requests for materials should be addressed to cjh275@cornell.edu

262

Text 14

1   **Methods**

2   Mechanical Characterization and Damage Assessment in Cancellous Bone

3   This study examined human vertebral cancellous bone (n=44 cancellous bone specimens from 10

4   male and 8 female donors, 62-92 years of age years of age) as reported in two prior studies [11,12]. Cyclic

5   loading was applied to a specified increase in cyclic strain and expressed as the average portion of the

6   fatigue life (N/N_f) using a previously identified empirical model (Fig. 1a).

7   Samples of human vertebral cancellous bone were acquired from the lumbar vertebrae of

8   deceased donors (tissue source NDRI). The donors had no history of metabolic bone disease or cancer.

9   The biomechanical analysis included cancellous bone from the third lumbar vertebral bodies of 16

10   donors [11] and from the fourth lumbar vertebral bodies of 12 donors [12] . Cylindrical specimens, 8 mm in

11   diameter and 27 mm in length were collected in the cranial-caudal direction using a coring tool. Two

12   specimens were collected from each L3 vertebra and one specimen was collected from each L4

13   vertebrae resulting in a total of 44 specimens. Specimens were wrapped in saline soaked gauze and

14   stored in airtight tubes at -20 °C until mechanical testing. Bone marrow was removed with a low-

15   pressure water jet.

16   Mechanical characterization of high porosity cellular solids can be challenging as the individual

17   struts of the foam deform locally at the contact with loading platens resulting in end artifacts that

18   generate non-uniform strains within the gage length [18]. To avoid end artifacts, specimens were press fit

19   into cylindrical brass end-caps and secured with cyanoacrylate glue (Loctite 401, Newington, CT, USA).

20   Using this approach, loads are transferred to the specimen via shear at the specimen/endcap interface

21   thereby avoiding end artifacts. After being secured in end caps the bone specimens were stored

22   overnight at 4 °C and hydrated with saline soaked gauze to allow the glue to fully cure.

23   Specimens were placed in a servo hydraulic testing machine (858 Mini Bionix, MTS, Eden

24   Prairie, MN, USA) and loaded in cyclic compression at room temperature (23 °C) to induce damage.

25   During testing, hydration was maintained by placing a rubber membrane around the specimen

26   containing physiologically buffered saline (pH of 7.4). Strain was measured with a 25 mm extensometer

27   (MTS, Eden Prairie, MN, USA) attached to the specimen's end-caps and force was measured with a load

28   cell (100 lb capacity, SSM-100, Transducer Techniques, CA, USA). Prior to each bout of loading, ten

29   preconditioning cycles between 0 and 0.1% strain at a rate of 0.5% per second was applied. Fatigue

30   loading was applied using a 4 Hz haversine waveform cyclically between 0 N and a compressive load

31   corresponding to $\sigma = E_0 * 0.0035$ mm/mm, where σ is stress and E_0 is the initial Young's modulus of the

32   specimen (determined from the preconditioning cycles). Force and strain data were collected to calculate

33   Young's modulus (E), reduction in Young's modulus ($1 - E/E_0$), and maximum strain [11,12].

34   Specimens from the third lumbar vertebrae included five specimens that were not subjected to

35   fatigue loading [11]. Fatigue loading of the remaining specimens was stopped before failure by monitoring

36   the creep-fatigue curve, secant modulus, and hysteresis loops to stop loading at a predetermined

37   magnitude of cyclic strain. Fatigue loading was stopped at the start of the secondary phase, in the middle

38   of the secondary phase, and at different points within the tertiary phase. Six specimens from the third

39   lumbar vertebrae were loaded well beyond the start of the tertiary phase to 4% apparent strain.

40   Specimens were then stained for damage using lead-uranyl acetate. The number of cycles to failure (N_f)

41   was determined for specimens loaded to an apparent strain of 4%. For the remaining specimens, the

42   number of cycles to failure (N_f) was estimated using an empirical relationship between reduction in

43   Young's modulus and proportion of fatigue life [11].

44   Specimens from the fourth lumbar vertebrae were loaded in two separate bouts of cyclic loading

45   at room temperature (23 °C) [12]. The first bout of fatigue was stopped at the beginning of the tertiary

Methods 2

46   phase (Fig.1a), identified as a the rapid increase in accumulation of apparent strain [11]. Following the first

47   bout of cyclic loading, specimens with end caps were carefully removed and bulk stained in xylenol

48   orange solution (0.5 mM, Sigma Chemical Co., St. Louis, MO) to stain damage caused by the first bout

49   of loading. The specimens were carefully returned to the material testing device, and a second bout of

50   cyclic loading was applied, until the specimens reached 5% apparent strain [11]. Specimens were carefully

51   removed from the testing device and bulk stained in calcein solution (0.5 mM, Sigma Chemical Co., St.

52   Louis, MO) to stain damage generated during the second bout of loading. Specimens were then

53   embedded undecalcified in methyl methacrylate.

54   Damage accumulation in specimens from the third lumbar vertebral bodies was determined using

55   the lead uranyl acetate stain and x-ray microcomputed tomography (10 μm isotropic voxels). A global

56   threshold was used to identify regions of bone tissue and damage stain (see [11]). Damage generated in

57   specimens from the fourth lumbar vertebrae was determined using images obtained through serial

58   milling (for a complete review of serial milling procedure, we direct the reader to prior work [19,20]). Serial

59   milling achieved a 0.7 X 0.7 X 5.0 μm voxel size image of bone and each of the fluorescent markers of

60   microdamage. Tissue damage stained and visualized using these approaches includes both microscopic

61   cracks as well as regions of constrained microcracking (known as diffuse damage in the bone literature).

62   As described in prior studies, the amount of tissue damage was correlated with the maximum applied

63   strain during cyclic loading. The relationship between maximum applied strain and amounts of

64   microdamage was similar for both staining/visualization techniques (Extended Data Fig. S5).

65

66   Cancellous Bone Microarchitecture

67   Microarchitecture was assessed using specimen average measurements (BoneJ, bonej.org, [21], 21

68   μm isotropic voxel microcomputed tomography images collected prior to fatigue loading,

69   Supplementary Information Table S6) as well as morphological analysis of each individual trabecula

70   (Supplementary Information Table S7). Morphological analysis involved classifying each trabecula as

71   rod-like or plate-like based on Digital Topological Analysis (DTA) (Fig. 1C, ITS software, Columbia

72   University). Additionally, the orientation of individual trabeculae was determined as the angle from the

73   superior-inferior direction and classified as longitudinal ($0 \leq \beta \leq 30°$), oblique ($30 < \beta \leq 60°$), and

74   transverse ($60 < \beta \leq 90°$) (Fig.1d) [13,22].

75   The amount of damage on plate- or rod-like trabeculae and the amount of damage present on

76   trabeculae with each orientation (longitudinal, oblique or transverse) was determined using custom

77   scripts written for use with Matlab (Mathworks, Natick, MA, USA) and Amira (5.3 Visage Imaging, San

78   Diego, CA, USA).

79   Failure of cancellous bone has been referred to as accumulation of failed trabeculae [23,24]. Here

80   we consider failure of a trabecula to occur when at least 10% of the volume of the trabecula includes

81   microdamage [25]. To understand patterns in failure of individual trabeculae, we report the proportion of

82   failed plate-like trabeculae (# failed plate-like trabeculae/ # plate-like trabeculae), and the proportion of

83   failed rods (Extended Data Fig. S1, #failed rod-like trabeculae/ # rod-like trabeculae).

84

85   <u>Additive Manufacturing of Modified Cancellous Bone Microstructures</u>

86

87   Microcomputed tomography images of a subset of cancellous bone samples (n=5, 10 µm voxel

88   images, 8 mm diameter, ~20mm length) [11,12] that had been collected before mechanical loading were

89   modified digitally by adding material to the surface of transverse rod-like trabeculae to three different

90   amounts: +60 µm (+120 µm strut thickness, 45% ± 14% increase in rod thickness), +20 µm (+40 µm in

91   rod thickness, 20% ± 5% increase in strut thickness) or no modification (original geometry). A high-

Methods 4

92   resolution stereolithography system (M1, Carbon, USA) was used to generate three-dimensional models

93   of the modified and unmodified microstructures from a urethane methacrylate polymer resin (UMA 90,

94   Carbon, USA, E = 2 GPa, [17]) at 1.5 times isotropic magnification (12 mm diameter, ~30 mm length).

95   The accuracy of the printed geometries was confirmed through direct comparison of the three-

96   dimensional .stl image to a microcomputed tomography image of the printed model (Supplementary

97   Information Table S7. Morphological analysis of each individual trabecula was analyzed for the three-

98   dimensional printed specimens (Supplementary Information Table S8).

99   Mechanical characterization of models of cancellous bone generated through additive

100   manufacturing was performed as described above. Specimens were submitted to cyclic fatigue loading

101   from zero to a normalized initial compressive stress magnitude σ/E_0 corresponding to 9500 $\mu\varepsilon$, 6500 $\mu\varepsilon$

102   or 4500 $\mu\varepsilon$ until failure (4% applied strain, Extended Data Fig. S3).

103   Damage in polymer specimens was identified using a radio opaque dye penetrant. Samples were

104   soaked for 24 hours at room temperature (23 °C) in the dye penetrant containing 250 g zinc iodide, 80

105   ml distilled water, 80ml isopropyl alcohol and 1 ml Kodak photo solution [26]. Samples were left to dry

106   for 12 hours to remove any excess dye prior to image acquisition using x-ray microcomputed

107   tomography (10 μm) [27].

108

109   Design and Manufacturing of Bone-like Architectured Material

110   Bone-like microarchitectures derived from the octet truss were designed in ABAQUS/CAE. The

111   length of the octet truss was elongated along one axis (the longitudinal axis) by 40% so that struts were

112   oriented 60 degrees from the transverse plane, thereby mimicking longitudinal elements seen in

113   cancellous bone. To further match the architecture of the cancellous bone, 6 plates were added per unit

114   octet. Transversely isotropic supercells were created from unit cells in which plates were included in

115   either the upper or lower half of each unit cell (Fig. S4). The resulting supercell achieved porosity,

116   transverse volume fraction, longitudinal volume fraction and plate volume fraction similar to the

117   cancellous bone specimens. These "supercell" structures were then exported as .stl files from the

118   ABAQUS/CAE sketcher and used for the 3D printing process.

119

120   Finite Element Modeling

121   Simulations were performed using ABAQUS/Standard. Models were meshed with C3D8 brick

122   elements (1.5 million/model) and quasi-static analyses were carried out for cyclic compressive loading

123   consistent with the same strain that was applied during experiments. The material was assumed to be

124   elastic-perfectly plastic with an initial Young's Modulus of 600 MPa and a yield stress of 26 MPa. The

125   structure was loaded under displacement-control along the loading axis with rollers on the other end and

126   free boundary conditions on all other sides. Simulations were run for 5 to 25 compression loading-

127   unloading cycles. Simulations were performed on a high performance computing cluster consisting of

128   10-core Intel Xeon-E5 processors. Inelastic dissipation was extracted from each model at the end of all

129   loading cycles.

130   To characterize the primary deformation mechanism within each model (bending dominated or

131   stretching dominated) the stress triaxility was determined at each point within the model. Stress triaxility

132   is defined as:

$$Triaxiality = -\frac{p}{q}$$

134   where p is the hydrostatic stress, defined as positive when stress is compressive and q is the vonMises

135   stress. By this definition, points under uniaxial tension would have a triaxiality of +0.33, and points

136   under pure uniaxial compression would have a triaxiality value of -0.33. Histograms summarizing the

137   values of stress triaxility within microstructures (Fig S4) under longitudinal compression show the

138   deformation behavior for each architecture. As expected, the octet shows only stretching deformation

139   (large peaks only at +0.33 or -0.33). The cancellous bone microstructure shows a high amount of

140   bending behavior (uniform distribution of triaxiality throughout with peaks at +0.33 and -0.33) and the

141   bone-like architectures show a combination of bending and stretching deformation behavior.

142

143   <u>Statistical Treatment</u>

144   A multivariate correlation analysis was used to identify trends between measures of damage,

145   changes in mechanical properties and volume-averaged measures of bone microarchitecture (Extended

146   Table S1). Others have shown that the amounts of microdamage formed during fatigue loading was

147   associated with maximum applied strain and reduction in Young's modulus and was not related to

148   volume-averaged measures of microarchitecture [11]. A backward elimination was performed using a

149   linear mixed model with fixed effects to identify aspects of trabecular microstructure that were

150   associated with the accumulation of fatigue damage. Donor was included as a random effect to take into

151   account the use of multiple specimens from each donor.

152   To examine the pattern of failure of discrete trabeculae observed during fatigue loading, an

153   ANCOVA was used to test for differences in the relationship between reductions in Young's modulus

154   and the number of failed plate- and rod-like trabeculae. An ANOVA was used to test for differences in

155   the number of failed trabeculae in each orientation (longitudinal, oblique, transverse) and post-hoc

156   comparisons were performed using Tukey HSD test.

157   A Generalized Least squares Model (GLM) was used to identify the empirical relationship

158   between stress amplitude (σ/E_0), the transverse volume fraction (ψ), and number of cycles to failure (N_f,

159   Equation 2). To account for differences in the number of samples for each microstructure (1-2

160 specimens per microstructure) microstructure was included as a random effect using REML. Statistical

161 tests were conducted using JMP 12 (SAS Institute Inc., Cary, NC, USA).

162

163 **Data and materials availability:** The data that support the findings of this study are available from the

164 corresponding author upon reasonable request.

165

166 **References**

167 18 Keaveny, T. M., Pinilla, T. P., Crawford, R. P., Kopperdahl, D. L. & Lou, A. Systematic and

168 random errors in compression testing of trabecular bone. *J. Orthop. Res.* **15**, 101-110 (1997).

169 19 Slyfield, C. R., Tkachenko, E. V., Wilson, D. L. & Hernandez, C. J. Three-dimensional dynamic

170 bone histomorphometry. *J. Bone Miner. Res.* **27**, 486-495, doi:10.1002/jbmr.553 (2012).

171 20 Slyfield, C. R., Jr. *et al.* Three-dimensional surface texture visualization of bone tissue through

172 epifluorescence-based serial block face imaging. *J Microsc* **236**, 52-59, doi:10.1111/j.1365-

173 2818.2009.03204.x (2009).

174 21 Doube, M. *et al.* BoneJ: Free and extensible bone image analysis in ImageJ. *Bone* **47**, 1076-

175 1079, doi:S8756-3282(10)01441-9, doi:10.1016/j.bone.2010.08.023 (2010).

176 22 Liu, X. S., Sajda, P., Saha, P. K., Wehrli, F. W. & Guo, X. E. Quantification of the roles of

177 trabecular microarchitecture and trabecular type in determining the elastic modulus of human

178 trabecular bone. *J. Bone Miner. Res.* **21**, 1608-1617 (2006).

179 23 Fyhrie, D. P. & Schaffler, M. B. Failure mechanisms in human vertebral cancellous bone. *Bone*

180 **15**, 105-109 (1994).

181 24 Fields, A. J. *et al.* Vertebral fragility and structural redundancy. *J. Bone Miner. Res.* **27**, 2152-

182 2158, doi:10.1002/jbmr.1664 (2012).

183   25   Fang, G., Ji, B., Liu, X. S. & Guo, X. E. Quantification of trabecular bone microdamage using

184   the virtual internal bond model and the individual trabeculae segmentation technique. *Comput*

185   *Methods Biomech Biomed Engin* **13**, 605-615, doi:10.1080/10255840903405660 (2010).

186   26   Schilling, P. J., Karedla, B. P. R., Tatiparthi, A. K., Verges, M. A. & Herrington, P. D. X-ray

187   computed microtomography of internal damage in fiber reinforced polymer matrix composites.

188   *Compos Sci Technol* **65**, 2071-2078, doi:10.1016/j.compscitech.2005.05.014 (2005).

189   27   Yu, B., Bradley, R. S., Soutis, C., Hogg, P. J. & Withers, P. J. 2D and 3D imaging of fatigue

190   failure mechanisms of 3D woven composites. *Compos Part a-Appl S* **77**, 37-49,

191   doi:10.1016/j.compositesa.2015.06.013 (2015).

192